AIAA JOURNAL
Vol. 44, No. 9, September 2006

Coanda Wall Jet Calculations Using One- and Two-Equation Turbulence Models

A. Gross* and H. F. Fasel†
University of Arizona, Tucson, Arizona 85721

DOI: 10.2514/1.3506

The wall jet over a convex surface, the Coanda wall jet, has many potential technical applications, such as circulation control of airfoils. Reynolds-averaged Navier–Stokes is a potentially very powerful tool for Coanda wall jet calculations. A number of common linear eddy-viscosity turbulence models were used for Reynolds-averaged Navier–Stokes calculations of a turbulent Coanda wall jet experiment. Calculations were also carried out with an explicit algebraic stress model. The differences in the computed results were shown to be large depending on what turbulence model was employed. The k–ω model was then employed for three-dimensional Reynolds-averaged Navier–Stokes calculations where the downstream evolution of streamwise vortices in the turbulent wall jet was studied for various spanwise wavelengths and forcing amplitudes. It was found that a centrifugal instability of the turbulent mean flow may lead to the streamwise growth of longitudinal vortices. Beyond a certain disturbance amplitude threshold the relative phase of the vortices had a noticeable impact on the amplification rates and the mean flow characteristics were affected by the added wall normal momentum exchange.

Nomenclature

A	=	forcing amplitude
b	=	nozzle exit slot width
D	=	Coanda cylinder diameter
$G\ddot{o}$	=	Görtler number
k	=	turbulent kinetic energy, spanwise mode
p	=	static pressure
R	=	Coanda cylinder radius
S	=	strain rate tensor
Tu	=	turbulence intensity
v	=	velocity
W	=	shear rate tensor
y	=	wall-normal coordinate
y_2	=	jet half-width
z	=	spanwise coordinate
β	=	spanwise wave number
Γ	=	total circulation
δ_{ij}	=	Kronecker symbol
ε	=	dissipation rate of k
ϑ	=	downstream coordinate
λ	=	wavelength
μ	=	dynamic viscosity
ν	=	kinematic viscosity
ρ	=	density
τ	=	Reynolds stress tensor
Φ	=	forcing phase
ω	=	turbulent specific dissipation, vorticity

Subscripts

i, j, k	=	spatial coordinates
jet	=	nozzle exit conditions
max	=	maximum in y
r	=	radial
T	=	turbulent
tot	=	total
z	=	spanwise
ϑ	=	streamwise, circumferential

Presented as Paper 2003-4020 at the 33rd AIAA Fluid Dynamics Conference and Exhibit, Orlando, FL, June 23–26, 2003; received 1 July 2003; revision received 24 April 2006; accepted for publication 4 May 2006. Copyright © 2006 by the authors. Published by the American Institute of Aeronautics and Astronautics, Inc., with permission. Copies of this paper may be made for personal or internal use, on condition that the copier pay the $10.00 per-copy fee to the Copyright Clearance Center, Inc., 222 Rosewood Drive, Danvers, MA 01923; include the code $10.00 in correspondence with the CCC.

*Research Assistant Professor, Member AIAA.
†Professor, Member AIAA.

Introduction

THE wall jet over a convex surface, the Coanda flow, is a potentially far more efficient way of generating an aerodynamic side force than a reaction nozzle. The streamline curvature causes the static wall pressure underneath the attached wall jet to be below ambient pressure, resulting in an aerodynamic force on the cylinder. The no tail rotor (NOTAR) helicopter is an existing and successful application. Circulation control airfoils, where a Coanda surface is situated at the trailing edge of a conventional airfoil, promise an increase in low-speed maneuverability when compared with traditional airfoils. They could also be used for short takeoff and landing and hingeless maneuvering of airplanes. The physical mechanisms involved in keeping the jet attached are, however, not well understood. Correct predictions of the spreading rate of the jet, which is dependent on the momentum exchange between jet and surrounding fluid, are essential. Better understanding of the relevant mechanisms would allow effective control and manipulation of the Coanda wall jet flow. This, in turn, could lead to an increased use of Coanda flows in technical applications.

The particular geometry chosen for the current investigations, a circular cylinder with a Coanda wall jet (Fig. 1), was investigated extensively in experiments by Wygnanski and coworkers [1–5]. In the experiments, the curved wall jet was found to spread faster than the plane wall jet. Two-point spatial cross-correlation measurements revealed the existence of large-scale streamwise structures [2–5]. Particle image velocimetry (PIV) combined with a pattern matching algorithm were employed to identify the structures as streamwise vortices [2–4]. These vortices appeared to increase the turbulent momentum exchange. The cross-correlations did, however, only show a weak minimum [5], indicating weak longitudinal structures. By placing a row of vortex generators along the span of the nozzle lip the coherence of the structures could be increased. This in turn lead to an earlier separation [3,4]. Neuendorf and Wygnanski also reported self-similarity of the streamwise velocity profiles up to $\vartheta = 180$ deg [1]. Here, the angular distance from the nozzle lip, ϑ, is used as a measure for the downstream distance. For $\vartheta > 180$ deg, the profiles began to deviate from the self-similar profiles in the inner region (between wall and velocity maximum) and the wall shear was lowered. Experiments carried out by Pajayakrit and Kind [6]

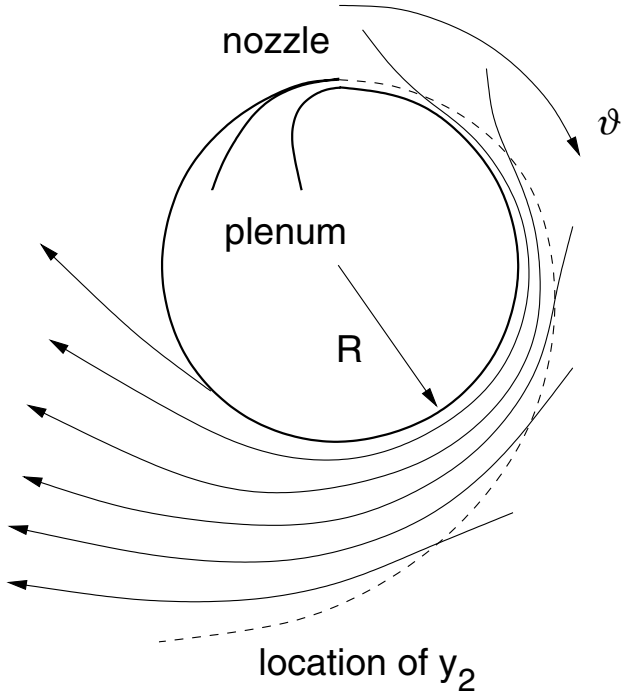

Fig. 1 Schematic of Coanda wall jet experiments by Wygnanski and coworkers [1–5].

provided further supporting evidence that streamwise coherent structures may be maintained by a curved turbulent wall jet. The downstream meandering of the structures could be prevented by placing pieces of thin adhesive tape on the nozzle lip. It was also found that exchanging the nozzle lip lead to an entirely new pattern of streamwise vortices.

Likhachev et al. [5] performed a linear stability theory (LST) analysis with respect to a centrifugal instability for the turbulent mean flow data as obtained from the experiments by Wygnanski et al. [1–5]. When the LST analysis was performed in the classical manner of Görtler, the experimental mean flow was only marginally unstable with very low amplification rates of the streamwise disturbances. Joshi and Tumin [7] carried out a linear and nonlinear stability analysis for the same flow. The linear analysis overestimated the growth rates when compared with the nonlinear analysis. It was shown that the initial conditions influence the neutral point locations but not the results farther downstream. It was also shown that streamwise vortices may shift the maximum of the velocity profile away from the wall.

A general discussion of Görtler vortices can be found in the survey paper by Saric [8]. The Görtler instability can occur for boundary layer flows over concave surfaces and for wall jet flows over concave and convex surfaces. The Görtler vortex problem is a nonlinear, nonparallel, convective instability in which the flow cannot be decoupled into a base flow and a disturbance flow. The location of the neutral point strongly depends on the location and the type of the upstream disturbances. Numerous publications are available regarding the growth of longitudinal vortices in laminar boundary layers over concave surfaces. A very detailed experimental investigation of the growth of longitudinal vortices and their role in the transition scenario of a concave laminar boundary layer was presented by Swearingen and Blackwelder [9]. A direct numerical simulation (DNS) of the growth of longitudinal structures in a curved laminar boundary layer was performed by Liu and Domaradzki [10]. Their interest was in the role of longitudinal vortices in the transition process. The numerical findings support the experimental results by Swearingen and Blackwelder [9].

Tani [11] was among the first to report on longitudinal vortices in a turbulent boundary layer along a concave wall. In his experiments he observed regularly spaced spanwise modulations of the velocity profiles which he attributed to a Görtler instability mechanism. Moser and Moin [12] performed DNS of a curved turbulent channel flow to reveal the effects of curvature in wall-bounded turbulent flows. They found stationary Görtler vortices which had a significant impact on the mean Reynolds shear stress and which enhanced the asymmetry of the channel flow. In strongly curved boundary layers the curvature effect on the turbulence characteristics is significant. For a curvature of $\delta/r = 0.1$ (where δ is the displacement thickness and r is the curvature radius) the turbulence intensities and shear stresses can, in some instances, be twice as large for the curved case than for the straight case [12].

Only few direct numerical simulations (DNS) of turbulent wall jets on curved surfaces are reported in the literature. This is partially due to the large range of length and time scales encountered in these flows. Resolving all scales of turbulent motion while still capturing the low frequency characteristics and spatial dimensions of the relevant coherent structure of the turbulent wall jet is computationally very challenging. Wernz et al. [13,14] performed 3-D DNS of the attached flow region of the Coanda wall jet experiment by Wygnanski and coworkers [1–5]. When the temporal mean of the DNS data was computed, longitudinal coherent structures became visible. It was shown that the intensity of these structures can be enhanced by steady forcing [14]. The DNS results also suggested that spanwise coherent structures can arise as a consequence of the inflection point of the wall jet velocity profile. This was shown earlier for the plane wall jet [15].

Reynolds-averaged Navier–Stokes (RANS) can be employed for dramatically lowering the computational cost. Pajayakrit and Kind [16] employed the Baldwin–Lomax and three two-equation linear eddy-viscosity models (LEVM) for calculating plane and curved turbulent wall jets. The model constants had to be tuned to obtain a better agreement of skin friction and spreading rate with the experimental data. It was pointed out that the Boussinesq–approximation (B–A) predicts zero Reynolds shear stress at the velocity peak whereas the zero shear-stress location in wall jets occurs substantially closer to the wall due to Reynolds-stress diffusion. For the curved wall jet, the nondimensional velocity profile predicted by the k–ε model matched the experimental profile whereas the profile predicted by the k–ω model had the velocity peak slightly too close to the wall.

It was shown already in 1981 that the use of LEVMs (or Boussinesq eddy-viscosity models) resulted in a significant underprediction of the influence of curvature when considering boundary layers on curved surfaces (cases 0231, 0232, and 0233 in [17], e.g., Launder et al., pp. 1390–1407, or Rodi et al., pp. 1495–1516). Specifically, the skin friction coefficient was overpredicted by LEVMs. Reasonable results for the curved boundary layer were obtained with algebraic stress models suggesting that a second-moment closure was needed when considering curved boundary layers. Simulations of a wall jet on a log-spiral with LEVMs (case 0261 in [17], e.g., Rodi et al., pp. 1495–1516) showed that the wall jet spreading rate was slightly overpredicted for the plane wall jet and increasingly underpredicted for the curved wall jet as the curvature increased.

Whereas curvature and rotation terms appear in full Reynolds-stress models, corrections need to be applied to LEVMs for them to make good predictions of curved turbulent flows. In the presence of curvature, the principal axes of the Reynolds-stress tensor are not aligned with the axes of the strain tensor. A curvature correction for the Spalart–Allmaras (S–A) model was proposed by Spalart and Shur [18]. An evaluation of curvature corrections for the S–A model and a two-equation explicit algebraic stress model (EASM) was performed by Rumsey et al. [19]. Simulations were carried out for a U-duct which was designed to minimize the streamwise pressure gradient such that the effects of curvature can be simulated without the complicating factor of streamwise pressure gradient. Velocity profiles and turbulent shear-stress predictions of the S–A model were greatly improved when the curvature correction was employed. The curvature correction for the EASM did, however, not considerably improve the results. An evaluation of the S–A model with and without curvature correction, the Menter shear-stress (SST) model, and a k-enstrophy model for circulation control airfoil simulations

was performed by Swanson et al. [20]. It was shown that the closest agreement with the experimental data was obtained with the S–A model corrected for curvature. Slomski et al. employed the standard k–ε model, a realizable k–ε model, and a full Reynolds-stress model for simulating an elliptic circulation control airfoil with Coanda cylinder at the trailing edge [21]. Only the Reynolds-stress model predicted spreading rate and separation location in accordance with the experiment. The spreading rate predicted by the k–ε models was too low, leading to a delayed separation of the wall jet. For one of the cases considered, a calculation with realizable k–ε model, the wall jet completely wrapped around the entire elliptic airfoil before separating.

This paper is organized in three parts: First, the governing equations, the numerical method, and the problem setup are explained. Second, various one- and two-equation turbulence models without curvature correction are employed for two-dimensional calculations of the turbulent Coanda wall jet experiment by Wygnanski and coworkers [1–5]. Third, one of these models is then employed for investigating the centrifugal instability of the turbulent mean flow with respect to longitudinal structures using three-dimensional RANS.

Numerical Method

Governing Equations

In the finite volume computational fluid dynamics (CFD) code used in the current investigations, the Favre-averaged compressible Navier–Stokes equations are solved in conservative form on structured grids. A variety of turbulence models was implemented for RANS of large Reynolds number flows. For the current investigations, the 1988 (in the following referred to as KW88) and the 1998 (KW98) version of the standard k–ω model by Wilcox [22] were employed. The 1998 version allows for improved predictions of free shear layer spreading rates. The Menter shear-stress transport (SST) model [23], which removes the k–ω model's sensitivity to the freestream value of the turbulence specific dissipation [24], the Lam–Bremhorst (L–B) low-Reynolds number k–ε model [25], and the Spalart–Allmaras (S–A) one-equation turbulence model [26] were considered as well. For the S–A model, the "tripping term" was omitted.

In the original formulations of the various turbulence models, the Boussinesq–approximation (in the following referred to as B–A) is employed for computing the Reynolds stresses,

$$\tau_{ij}^{T} = -\frac{2}{3}\rho k\delta_{ij} + 2\mu_T\left(S_{ij} - \frac{1}{3}v_{k,k}\delta_{ij}\right) \tag{1}$$

where $S_{ij} = 1/2(u_{i,j} + u_{j,i})$ and $W_{ij} = 1/2(u_{i,j} - u_{j,i})$ are the strain and shear rate tensor. Repeated indices indicate summations whereas commas in the subscript denote partial derivatives. The B–A assumes a linear relation between the strain tensor and the Reynolds-stress tensor. Alternatively, a second-moment closure, the explicit algebraic stress model (EASM) in the form proposed by Rumsey and Gatski [27],

$$\tau_{ij}^{T} = -\frac{2}{3}\rho k\delta_{ij} + 2\mu_T\left[\left(S_{ij} - \frac{1}{3}v_{k,k}\delta_{ij}\right) + a_2a_4(S_{ik}W_{kj} + S_{jk}W_{ki}) - 2a_3a_4\left(S_{ik}S_{kj} - \frac{1}{3}S_{kl}S_{kl}\delta_{ij}\right)\right] \tag{2}$$

is employed.

Discretization

The convective terms of the Navier–Stokes equations were discretized with a fifth-order accurate upwind scheme based on a weighted essentially nonoscillatory (WENO) extrapolation of the characteristic variables and the Roe scheme [28]. The convective terms of the turbulence model equations were discretized with a second-order accurate discretization (in the following referred to as O2) analogous to the symmetric total variation diminishing (TVD) scheme found in [29] or a numerically more robust first-order accurate upwind scheme (O1). Fourth-order accurate finite differences were used for the Navier–Stokes viscous terms and second-order accurate central differences were used for the turbulence equations viscous terms. The governing equations were advanced in time with a first-order accurate backward Euler scheme for steady flows or a second-order accurate Adams–Moulton method for time-dependent flows. The system of equations resulting from the implicit time-integration was solved iteratively by a Newton iteration based on a line Gauss–Seidel algorithm. For steady RANS results only one iteration was carried out per time step. The convergence of the implicit method was monitored by considering the L_2-norm of the residual of the governing equations. For time-dependent problems the equations were advanced to the next time step when the L_2-norm dropped below 1.

Problem Setup

Case Description

The Coanda flow experiment by Wygnanski and coworkers [1–5] was chosen for the calculations presented in this paper. A sketch of the geometry is shown in Fig. 1. Fluid contained in the plenum and replenished from a pressure tank accelerates in a nozzle and is issued as a wall tangential jet into a quiescent ambient. Because of wall-normal mixing, ambient fluid is entrained into the wall jet. The wall jet thickness grows in the downstream direction while the maximum velocity decays, eventually leading to flow separation. In the experiment, the Coanda wall jet detached from the cylinder around $\vartheta = 240$ deg. The radius of the cylinder was $R = 0.1016$ m, the slot width (nozzle lip to cylinder surface) was $b = 2.34 \times 10^{-3}$ m, and the jet exit velocity was $v_{\text{jet}} = 48$ m/s. This results in a Newman Reynolds number [1] of

$$Re_N = \frac{v_{\text{jet}}\sqrt{bR/2}}{\nu} = 33,000 \tag{3}$$

and a Reynolds number based on jet exit velocity and cylinder diameter of

$$Re_D = \sqrt{\frac{8R}{b}}Re_N = 615,032 \tag{4}$$

The jet exit Reynolds number based on slot width and jet exit velocity was about 7000. At this Reynolds number, transition in a plane wall jet can be expected to be complete for $x/b \approx 20$ [30]. The transition process is, however, strongly dependent on the nozzle exit conditions. All lengths are nondimensionalized by the cylinder diameter. Velocities are nondimensionalized by the jet exit velocity. The gas is assumed to be ideal with Prandtl number, $Pr = 0.72$, and ratio of specific heats, $\gamma = 1.4$. For our present calculations, the ambient and jet exit temperature were assumed to be 300 K and the jet exit Mach number, M, was set to 0.25. Also, the fluid at the nozzle exit was assumed to have ambient density and static pressure. To save computer time it was decided to not model the plenum chamber and the nozzle but to prescribe a velocity profile at the jet exit location. After consulting with the experimentalists it was agreed on that a top-hat velocity profile (with negligible boundary layer thickness) was in reasonably close agreement with measured velocity profiles at the nozzle exit [1]. Because quantitative measurements of the ambient and jet exit turbulence quantities were not available, it was decided to assume a very low turbulence intensity in the ambient and for the jet at the nozzle exit location. For RANS calculations with the k–ω models and the SST model, an eddy viscosity (nondimensionalized with the molecular viscosity) of $\mu_T/\mu = 10^{-6}$ and a turbulent Mach number of $M_T = 10^{-5}$ were prescribed at the ambient boundary and at the jet exit. This was necessary for obtaining solutions that were independent of the freestream value of ω [24]. The corresponding jet turbulent intensity was $\text{Tu} = \sqrt{1/3}M_T/M = 2.3 \times 10^{-5}$ and the turbulence length scale was $l_T/D = \sqrt{2/3}\mu_T/\mu/(Re\,\text{Tu}) = 5.7 \times 10^{-8}$. For the S–A model, only one quantity needs to be prescribed. Instead of using

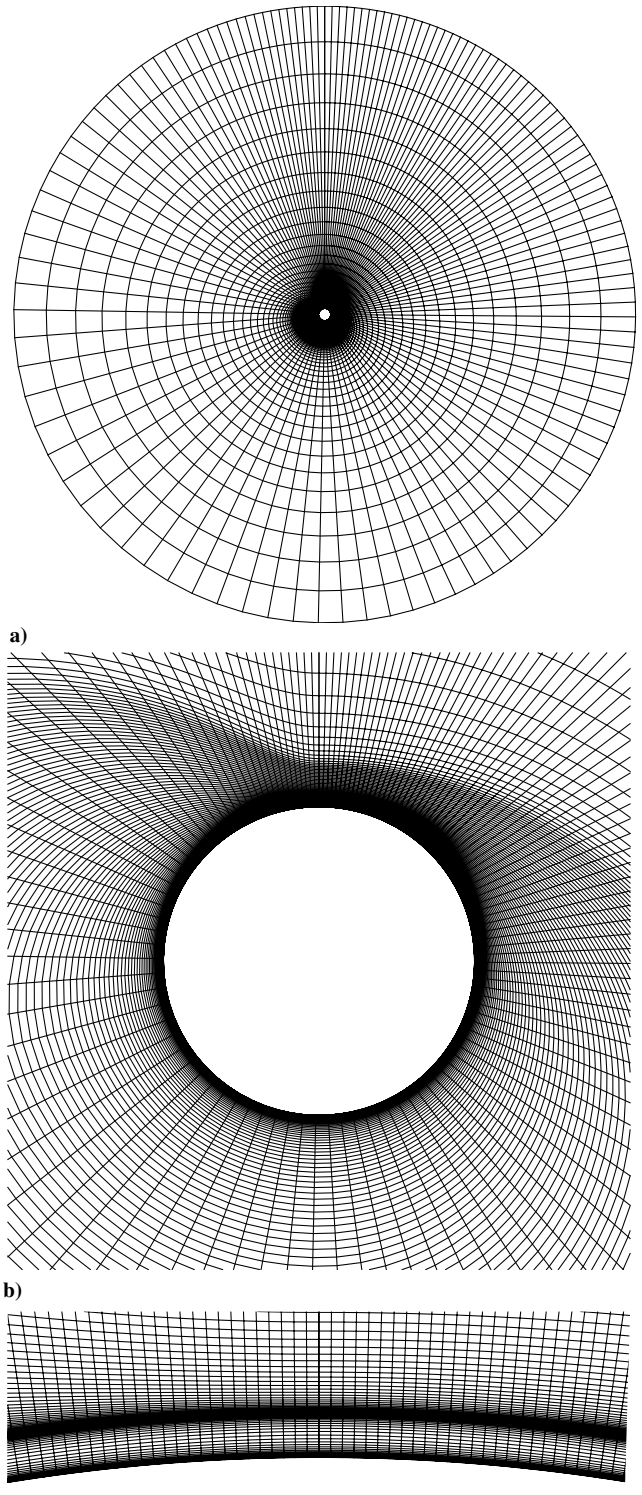

Fig. 2 Details of fine grid used for RANS results. a) Total grid, b) close-up of cylinder, and c) close-up near nozzle exit. For clarity, only every fourth line is shown in the azimuthal direction for a) and b).

laminar inflow conditions and tripping the model [26] the normalized eddy viscosity at the nozzle exit was set to 0.01, resulting in a turbulent Coanda wall jet. For the k–ε model the jet exit turbulence intensity was set to 1% and the turbulence length scale was assumed to be identical to the nozzle exit slot width, resulting in $M_T = 0.0043$ and $\mu_T/\mu = 86.7$. For the ambient, $M_T = \mu_T/\mu = 0.001$ were prescribed. When the turbulence intensity at the jet exit was reduced to 0.1%, the wall jet remained laminar in the simulation (not shown). When the same turbulent quantities were used with the k–ω models, an unrealistic buildup of eddy viscosity could be observed in the jets outer layer (not shown). The inner layer or region of the wall jet is defined as the region between the wall and the location of the velocity maximum whereas the outer region is defined as the region between the location of the velocity maximum and the ambient. The distance from the wall where the local wall tangential velocity in the wall jet's outer region attains half of its maximum value is called half-width and denoted as y_2.

Computational Grid

Different from earlier approaches [31,32], a one-block radial grid topology was chosen for the following reasons: Areas of high grid distortion which degrade the accuracy of the solution are avoided and the efficiency of the numerical method is improved as the line relaxation method can operate over the entire computational domain. A fine and a coarse computational grid were generated. The fine grid had 500 cells around the cylinder and 130 cells in the wall-normal direction. The coarse grid had 250 times 97 cells. Both grids feature significant grid point clustering near the wall and close to the nozzle exit. The streamwise resolution of these grids close to the nozzle was likely insufficient for fully resolving the Kelvin–Helmholtz instability in the high-shear region near the nozzle exit. This was not a concern because it was decided that a detailed and accurate prediction of the transition process was beyond the scope of the present investigations. Details of the fine grid are shown in Fig. 2. The viscous sublayer was resolved in detail for both grids. The near wall grid resolution was smaller than 1 (Fig. 3a), the grid expansion ratio was nowhere larger than 1.2, the number of cells for $y^+ < 30$ was larger than 10 (Fig. 3b), and the number of cells for $y < y_2$ was between 30 and 40 for the coarse grid and between 40 to 50 for the fine grid. The total grid extent in the radial direction measured from the cylinder center was $25D$. It was found that for a smaller spatial extent of the computational grid, the predicted ambient velocity in the computational domain became dependent on the grid size (not shown). For the 3-D RANS calculations the 2-D RANS grid was extended in the spanwise direction (details are discussed later).

Boundary Conditions

At the nozzle exit (the inflow boundary of the computation), all flow quantities were prescribed, except for the static pressure, which was extrapolated from inside the computational domain (zero first derivative). The nozzle was assumed to have zero extent in the azimuthal direction. Admittedly, the wall-normal resolution on the back of the nozzle (Fig. 2c) was not sufficient for resolving the near-wall flow. The integral nature of the resulting corner flow was, however, captured (Fig. 4). Walls were considered to be adiabatic with k, $\partial\varepsilon/\partial y$, and $\tilde{\nu}$ being zero at the wall. Wilcox gives a relation for the dependence of ω on the wall distance y^+ in close vicinity of a hydraulically smooth wall [33]. This relationship was employed for computing the value of ω for the wall next cell. The computed value was then multiplied by 10 and prescribed as wall value for ω. In principle, for a perfectly smooth wall, ω becomes infinite at the wall. Prescribing arbitrarily large values of ω at the wall may result in accurate model predictions. It can, however, reduce the robustness of the numerical method. This procedure yields accurate results without compromising robustness. A characteristics-based boundary condition that enforces the ambient state was employed at the ambient boundary [34].

Results

2-D RANS Calculations

Table 1 summarizes the various 2-D RANS calculations performed. Unless indicated otherwise, the B–A was employed. The earliest separation was predicted with the k–ω models with B–A, followed by the k–ω models with EASM, the L–B model, and the SST model. With the S–A model, the jet wrapped around the cylinder more than once; this is in disagreement with the experiment. It will be shown later that earlier separation is a consequence of a larger

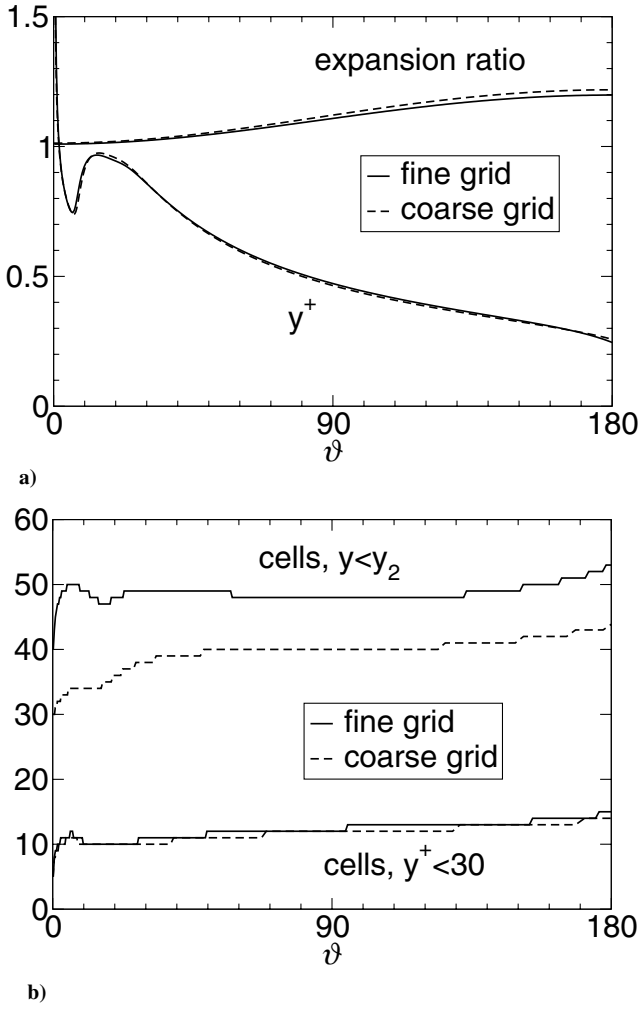

Fig. 3 Characteristics of computational grids. a) Wall grid resolution in wall units, y^+, and grid expansion ratio at wall. b) Number of grid cells covering wall distance $y^+ = 0 \ldots 30$ and $y = 0 \ldots y_2$. Results obtained with KW88 O1.

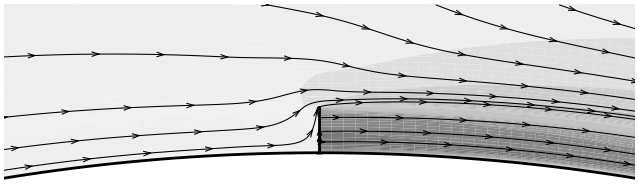

Fig. 4 Close-up near nozzle exit (same close-up as in Fig. 2c). Isocontours of total velocity and streamlines. Fine grid result with KW88 O1.

streamwise jet velocity decay and spreading rate. Because of the difference in time scales between the dynamics of the jet close to the nozzle exit and the ambient flowfield, 300,000–600,000 time steps with a step size of $\Delta t = 0.01$ had to be computed before the ambient flowfield became more or less steady. In some instances, unsteady vortices arose in the shear layer close to the nozzle exit as a consequence of the Kelvin–Helmholtz instability of the wall jet profile. A low-frequency flapping motion of the separated jet could be observed when the L–B model was employed.

A typical example of the ambient flow is shown in Fig. 5. Ambient air is sucked in from above, deflected around the cylinder, and ejected in a direction that is at an angle to the direction of the incoming fluid. The Coanda wall jet causes a circulation around the cylinder that results in an aerodynamic force and an inviscid ambient flowfield reminiscent of the flowfield around a rotating circular cylinder. Two large vortices are situated within the computational

Table 1 Overview of 2-D RANS calculations: grid resolution, accuracy of discretization of turbulence convective terms, and separation location (determined by zero skin friction of time mean)

Model	Grid	Discr.	Separation
KW88	Coarse	O1	206 deg
		O2	199 deg
	Fine	O1	196 deg
		O2	191 deg
KW98	Coarse	O1	216 deg
		O2	203 deg
	Fine	O1	205 deg
		O2	200 deg
KW98 EASM	Coarse	O1	216 deg
	Fine	O1	211 deg[a]
		O2	217 deg[b]
SST	Coarse	O1	257 deg
	Fine	O1	249 deg[a]
L–B	Coarse	O1	334 deg[c]
S–A	Fine	O1	——[d]

[a]Slight unsteadiness of flow near nozzle exit caused by shear layer instability.
[b]Unsteadiness of flow near nozzle exit.
[c]Slight unsteadiness of jet near separation (low-frequency flapping motion).
[d]Jet wraps around cylinder more than once.

domain, one to the left and one to the right of the cylinder. The left vortex induces a noticeable ambient velocity in the order of 2% of the jet exit velocity. In the vicinity of the cylinder in the inviscid flow regime the flow is accelerated to about 4% of the jet exit velocity. Isocontour plots of total velocity,

$$v_{\text{tot}} = \sqrt{v_\vartheta^2 + v_r^2} \tag{5}$$

are shown in Fig. 6. An instantaneous visualization of the transient flowfield is shown for the result with S–A model. The flowfields look qualitatively similar apart from the different separation locations and the slightly different jet spreading rates.

The streamwise variation of the wall pressure coefficient,

$$c_p = \frac{p - p_{\text{jet}}}{\frac{1}{2}\rho_{\text{jet}} v_{\text{jet}}^2} \tag{6}$$

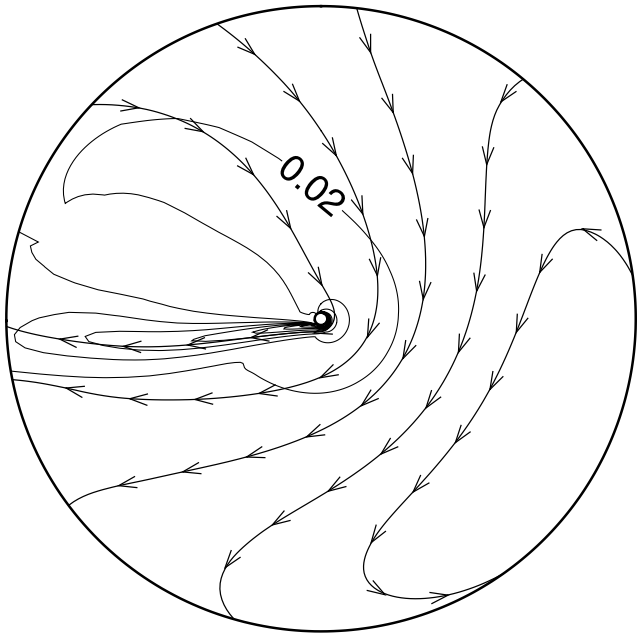

Fig. 5 RANS result obtained with KW88 O1 on fine grid. Streamlines and isocontourlines of total velocity (contour levels from 0 to 1 with increment 0.02).

is shown in Fig. 7. The streamline curvature of the attached wall jet necessitates a static pressure below ambient at the cylinder wall. With RANS the wall suction associated with the Coanda effect is overpredicted when compared with the experimental data. This discrepancy may be attributed to modeling deficiencies (this issue will be addressed in length later). In a separate investigation it was found that both the wall jet separation location and the wall pressure distribution are very sensitive to the ambient flowfield. An ambient velocity of only 1% of the jet exit velocity is sufficient for significantly altering the wall pressure distribution and noticeably affecting the separation location (Fig. 7). Similar effects may also be achieved by flow obstructions in the ambient.

To further analyze the data, measures for the jet velocity decay (the square of the inverse of the maximum jet velocity normalized by the jet exit velocity) and the jet spreading rate (the jet half-width normalized by the slot width) were compared with the experimental data [1–5] (Fig. 8). Because it was already noted that large deviations in both the separation location and the wall pressure distribution were predicted with the various turbulence models, the large scattering in the predicted velocity decay and spreading rates is not surprising. One possible explanation for the poor performance of the turbulence models is the fact that neither one of them explicitly accounts for curvature effects. It was shown by Rumsey et al. [19] that curvature terms can noticeably improve the predictive capability of the S–A model for curved flows. However, they also mentioned that curvature corrections for the EASM model did not considerably improve the model predictions. Hence, the impact of the flow curvature on the turbulence characteristics may not be the only explanation for the discrepancies between the RANS results and the experimental data.

When spreading rate and velocity decay are scaled such that they collapse on the experimental data at $\vartheta = 60$ deg (at this location the wall jet was found to be fully turbulent in the experiment [1]), the results seem to be in better agreement with the experimental data

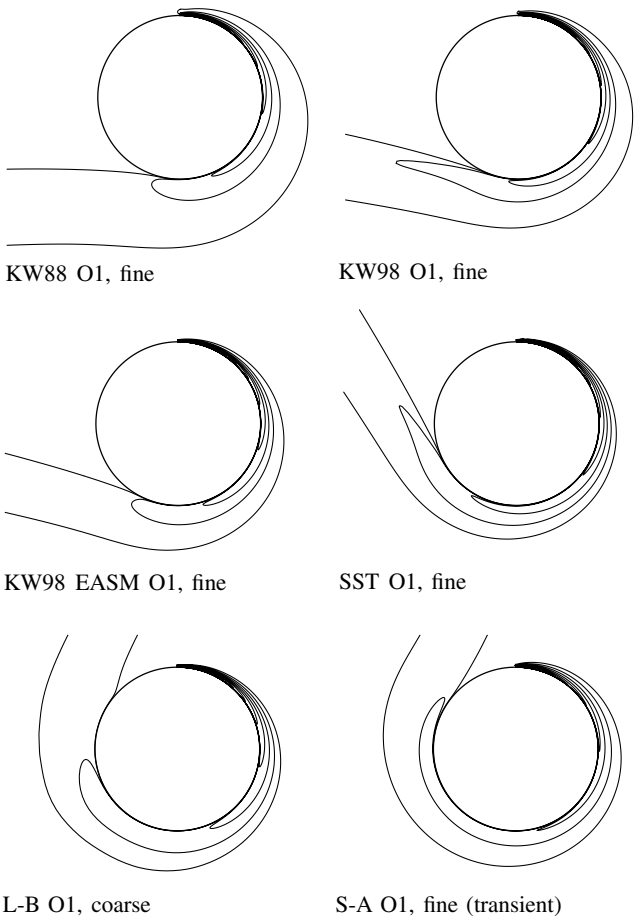

Fig. 6 Isocontourlines of total velocity (contour levels from 0 to 1 with increment 0.1) obtained from RANS calculations (Table 1).

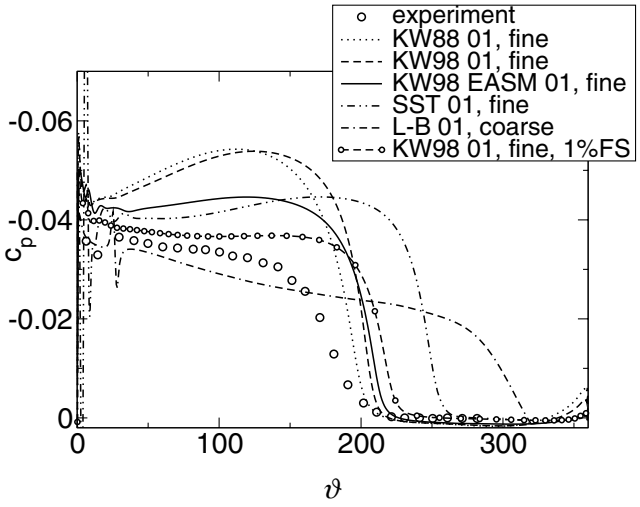

Fig. 7 Comparison of RANS prediction of wall pressure coefficient with experimental data [1]. All results are for quiescent ambient except for "KW98 O1, fine, 1%FS," where the ambient velocity is 1% of the jet exit velocity. The ambient flow is directed against the nozzle exit (the ambient flow is coming from the right).

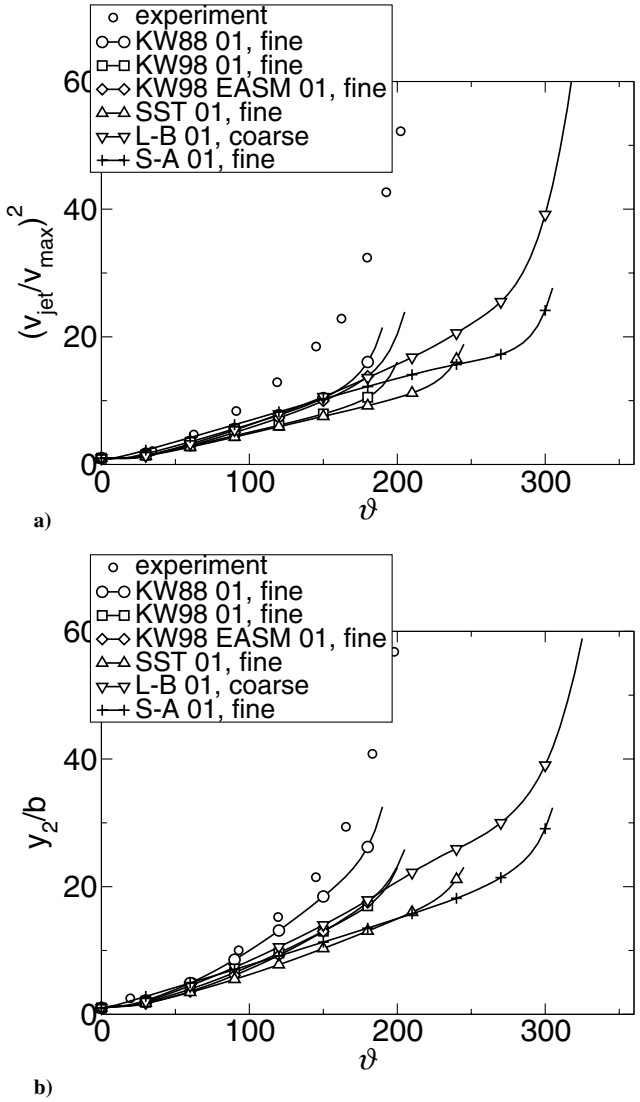

Fig. 8 Comparison of a) inverse of square of maximum jet velocity and b) wall jet half-width as obtained from RANS calculations with experimental data [1]. Result for S–A model is transient (data shown are for same time instant as in Fig. 6).

(Fig. 9). The scaling idea [13] was motivated by the fact that the transition process of the wall jet was not reproduced correctly in the calculations. This may result in a different wall jet velocity profile with different turbulent characteristics downstream of the transition point and influence the entire downstream development of the flow.

The wall jet velocity profiles were reported to be nearly self-similar up to $\vartheta \approx 180$ deg [1]. The following deviation from the self-similarity was attributed to streamwise vortices that increase mixing in wall-normal direction and appear to be the reason for the shift of the velocity maximum away from the wall for $\vartheta \geq 180$ deg. Results by Joshi and Tumin [7] support this conjecture. In principle, spanwise coherent structures could also exist in the wall jet and enhance the wall-normal mixing [13].

Wall-normal profiles of circumferential velocity are shown in Figs. 10 and 11a. The velocity profiles were scaled with the wall jet half-width and the velocity maximum [1]. The most noticeable deviation from the experimental data can be observed for the KW88 and KW98 models where the velocity maximum is predicted too close to the wall and the profile in the outer part of the wall jet is not full enough. Good agreement with the experimental data at $\vartheta = 60$ deg was obtained with the KW98 EASM, SST, and L–B models. At this location, the wall jet profiles were reported to be nearly self-similar, suggesting turbulence equilibrium [1]. At $\vartheta = 180$ deg, only the result obtained with the L–B model is in reasonable agreement with the experimental data. However, it should be kept in mind that the profiles were normalized and that the dimensional thickness of the wall jet at this location was significantly underpredicted by the L–B model (Fig. 8b).

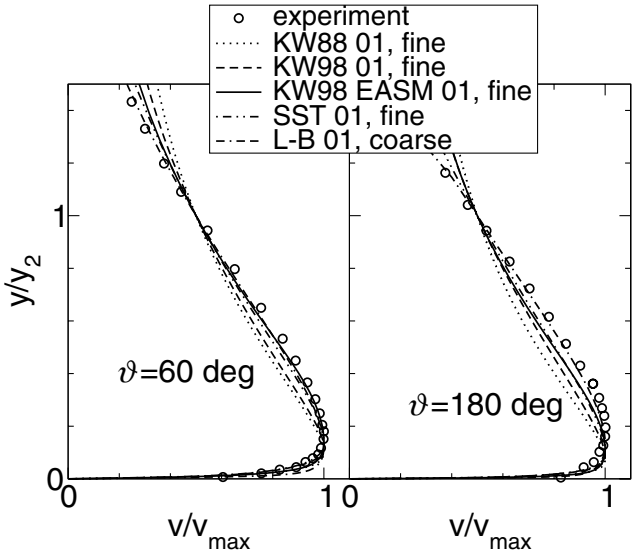

Fig. 10 Comparison of wall-normal profiles of streamwise velocity at $\vartheta = 60$ deg and $\vartheta = 180$ deg with experimental data [1].

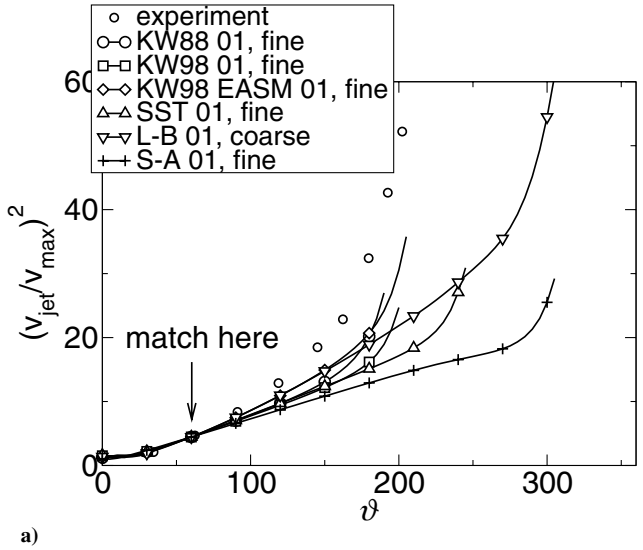

a)

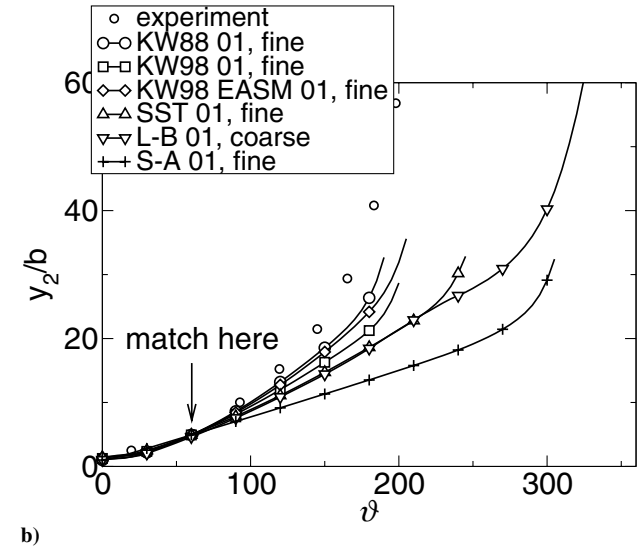

b)

Fig. 9 Comparison of a) inverse of square of maximum jet velocity and b) wall jet half-width as obtained from RANS calculations with experimental data [1]. Result for S–A model is transient (data shown are for same time instant as in Fig. 6). The RANS results were rescaled to match the experimental data at $\vartheta = 60$ deg.

The large deviation of the profiles of turbulence intensity,

$$\mathrm{Tu} = \sqrt{\frac{2}{3}k} \tag{7}$$

as shown in Fig. 11b is not surprising. The maximum of the turbulence intensity is approximately situated at the location of the inflection point of the velocity profile. The highest levels of turbulence intensity in the wall jet's outer layer were predicted with the KW88 and KW98 EASM models. Profiles of Reynolds shear stress are shown in Fig. 11c. The locations of zero shear stress approximately coincide with the locations of the velocity maxima. Again, the spread in the predicted results is large. In general, higher Reynolds-stress levels were predicted with the EASM when compared with results where the B–A was employed.

Finally, the impact of grid resolution and numerical accuracy (of the discretization of the turbulence convective terms) were studied for the KW88 model. The differences in predicted jet velocity decay and spreading rate are small (Fig. 12a). The velocity profiles almost collapse on each other (Fig. 12b). A slight variation of the turbulence intensity and Reynolds shear-stress profiles can be noticed. When also considering the predicted separation location (Table 1), it was concluded that the results showed sufficient grid convergence for the purposes of the present investigations.

3-D RANS Calculations

Because it was concluded from the experiments that streamwise coherent structures may have a considerable impact on the jet characteristics, it was decided to employ 3-D RANS for investigating the conditions for which the turbulent wall jet supports longitudinal vortices. To determine what spanwise extent of the computational domain was appropriate for the 3-D RANS calculations the following procedure was applied. The local Görtler number was computed from the 2-D RANS data,

$$G\ddot{o} = \frac{y_2 v_{\vartheta,\max}}{\nu_{T,\mathrm{av}}} \sqrt{\frac{y_2}{R}} \tag{8}$$

where ν_T is a locally averaged eddy viscosity. For the current results the quantity $\nu_T = \mu_T/\rho$ was averaged in the radial direction,

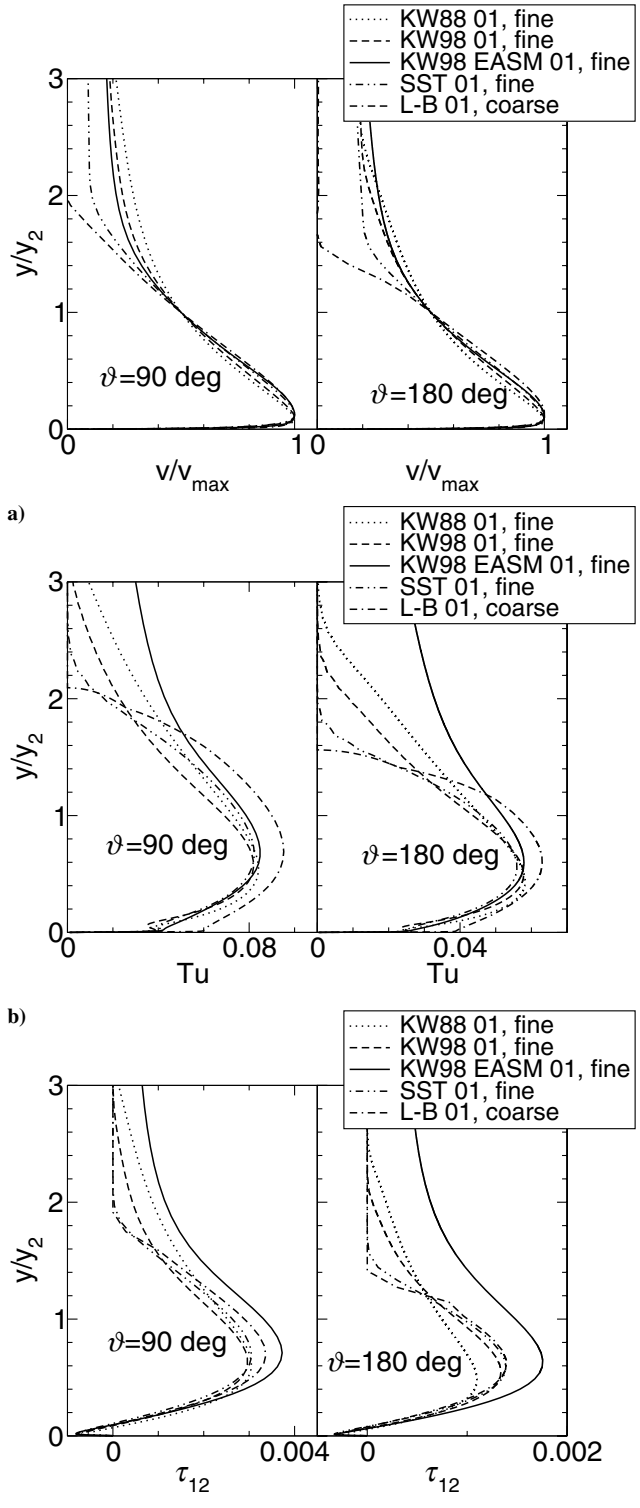

Fig. 11 Wall-normal profiles of a) streamwise velocity, b) turbulence intensity, and c) Reynolds shear stress at $\vartheta = 90$ deg and $\vartheta = 180$ deg.

$$\nu_{T,\mathrm{av}} = \frac{1}{y_{0.2}} \int_{y=0}^{y_{0.2}} \nu_T \, \mathrm{d}y \tag{9}$$

where $y_{0.2}$ is the wall distance of the point in the wall jet's outer layer where $\nu_T = 0.2\nu_{T,\max}$. Likhachev et al. [5] and Joshi and Tumin [7] also averaged the eddy viscosity for their stability analysis. In stability diagrams, the Görtler number is typically plotted against the spanwise wave number,

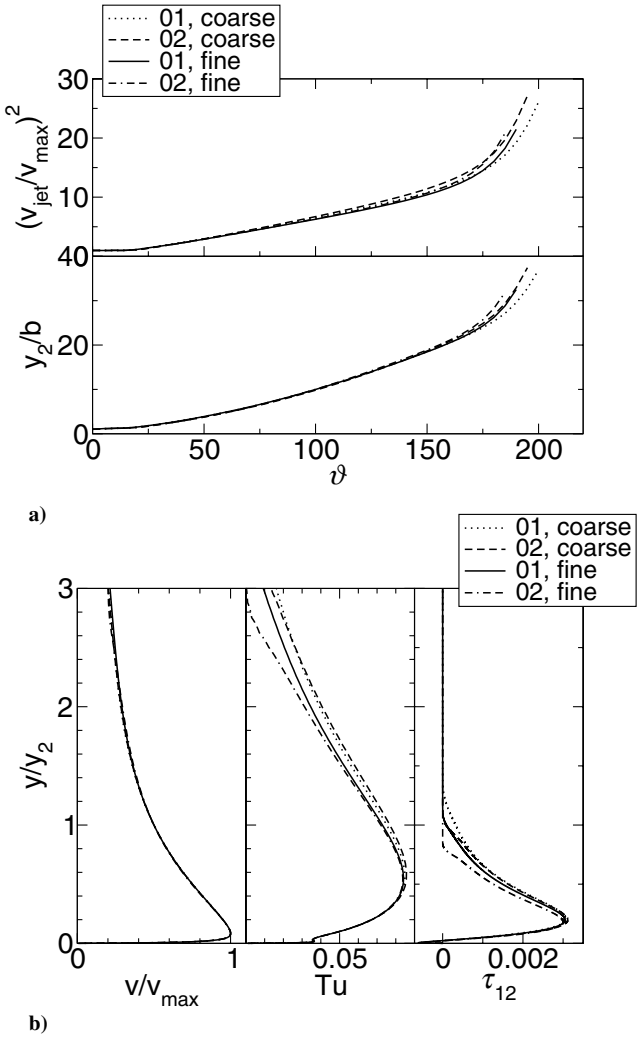

Fig. 12 a) Inverse of square of maximum jet velocity and wall jet half-width and b) profiles of streamwise velocity, turbulence intensity, and Reynolds shear stress at $\vartheta = 90$ deg.

$$\beta = 2\pi \frac{y_2}{\lambda_z} \tag{10}$$

which is dependent on the local half-width and the spanwise wavelength. For a given spanwise wave number, the flow becomes unstable when the Görtler number becomes larger than the neutral stability (or critical) Görtler number. A data fit for the neutral stability Görtler number in the stability diagram by Likhachev et al. (Fig. 3 in [5]) in the interval $1 \leq \beta \leq 4$ is

$$G\ddot{o}(\beta) = 5.239 - 5.212\beta + 3.164\beta^2 - 0.2356\beta^3 \tag{11}$$

For a fixed λ_z, the spanwise wave number becomes dependent on the local half-width, which is dependent on the downstream coordinate. Curves of the neutral stability Görtler number for several spanwise wavelengths can be plotted over the streamwise coordinate by obtaining the half-width from Fig. 8b, computing β from Eq. (10), and then computing the neutral stability Görtler number from Eq. (11). Results for the KW88 and KW98 model with B–A are shown in Fig. 13. Whenever the local Görtler number is larger than the local neutral stability Görtler number for a given wavelength λ_z, the flow becomes Görtler unstable with respect to disturbances with the same spanwise wavelength.

Because of the significantly larger levels of eddy viscosity predicted with the KW88 model when compared with the KW98 model, the local Görtler number is smaller with the KW88 model.

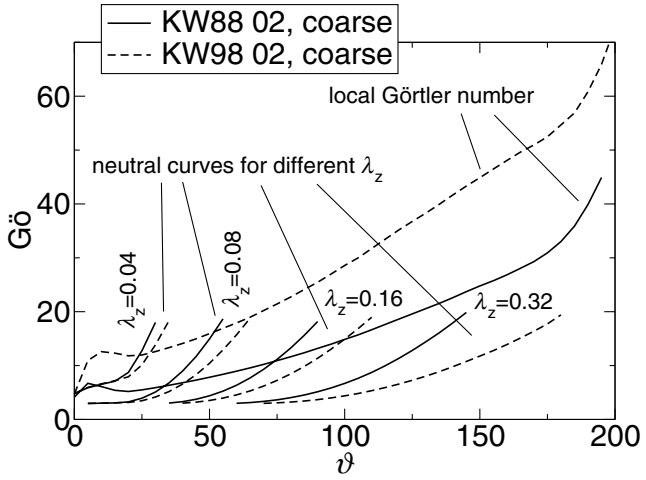

Fig. 13 Local Görtler number as computed from 2-D RANS results and curves of the neutral stability Görtler number [Eq. (11)] for different spanwise wavelengths in the interval $1 \le \beta \le 4$.

The following observations can be made for the KW88 model (Fig. 13): The flow is stable for disturbances with a spanwise wavelength smaller than 0.04. For $\vartheta > 33$ deg spanwise disturbances with $\lambda_z < 0.08$ will be damped, for $\vartheta > 74$ deg spanwise disturbances with $\lambda_z < 0.16$ will be damped, and for $\vartheta >$ 150 deg spanwise disturbances with $\lambda_z < 0.32$ will be damped. In essence, the wall jet is unstable with respect to small spanwise wavelengths close to the nozzle exit where the wall jet is thin, and unstable with respect to large spanwise wavelengths in the downstream part where the wall jet is thicker. In fact, one of the basic findings from both experiment [3–5] and theoretical analysis [5,7] is that the spanwise wavelength of the locally dominant spanwise disturbance is roughly equal to twice the local jet half-width. The reader must be reminded that the preceding comparison with stability theory results is of a qualitative nature only. It is, however, illustrative and aids in understanding the results obtained from the 3-D RANS investigations presented in the remaining part of the paper.

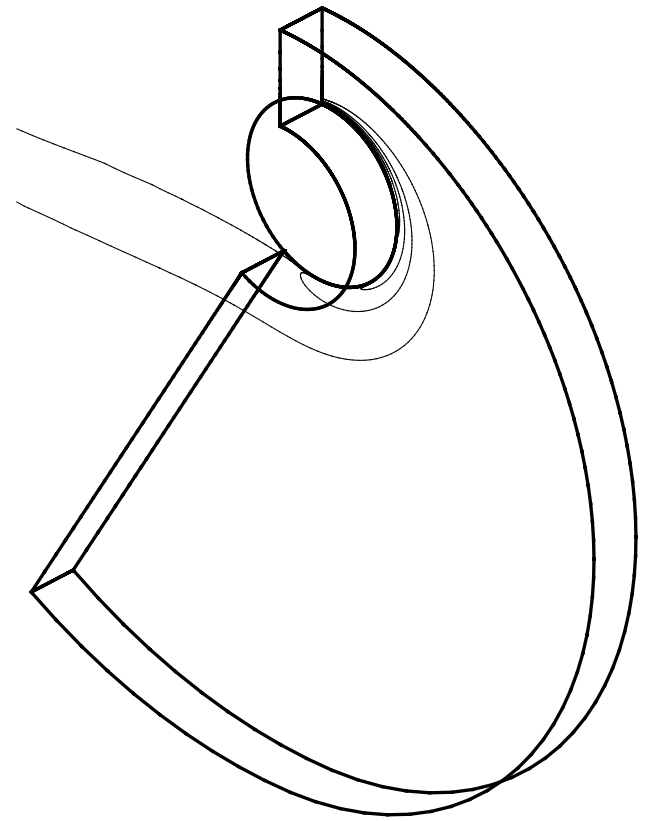

Fig. 14 Outline of computational domain used for 3-D RANS calculations overlaid on 2-D RANS result obtained with KW88 O2 on coarse grid. Shown are isocontourlines of total velocity.

From the previous results it was determined that a maximum spanwise wavelength of $\lambda_z \approx 0.3$ had to be expected for the following 3-D RANS investigations. The grid for the 3-D RANS calculations was generated by extending the 2-D grid (for the attached wall jet region) in the spanwise direction, z (Fig. 14). The spanwise grid extent, Δz, was 0.15 for the linear case and 0.3 (thus allowing spanwise wavelengths up to $\lambda_z = 0.3$) for the nonlinear cases (to be explained later). In both instances, 48 cells were evenly distributed in the spanwise direction (Table 2). For the linear case, symmetry (slip wall) was enforced at the spanwise boundaries. Because relative phase differences between the spanwise modes were studied for the nonlinear cases (to be explained later) the periodicity condition was employed at the spanwise boundaries for these cases. The total number of cells was 0.6 million. Unless noted otherwise, all 3-D RANS calculations were performed with KW88 model, B–A, and second-order accurate turbulence convective terms, because this combination resulted in the best prediction of wall jet half-width and velocity decay when compared with the experiments (Fig. 8).

Longitudinal vortices were generated at the nozzle exit and their development in the downstream direction was studied. The disturbances were introduced at the inflow boundary of the 3-D domain by superimposing a disturbance of the wall-normal (v_r) and spanwise (v_z) velocity components onto the wall jet profile,

$$v_r' = \sum_{k=1}^{k_{\max}} A_k \cos\left(\frac{2\pi k z}{0.3} - \phi_k\right) \sin\frac{\pi y}{b} \tag{12}$$

$$v_z' = -\sum_{k=1}^{k_{\max}} A_k \sin\left(\frac{2\pi k z}{0.3} - \phi_k\right) \sin\frac{2\pi y}{b} \tag{13}$$

where A_k and ϕ_k are the forcing amplitude and the phase of the spanwise mode k, respectively. One case with linear (small) and three cases with nonlinear (large) disturbance amplitudes were studied. The forcing parameters are listed in Table 3. Results from the linear case were compared with LST results by Likhachev et al. [5]. The nonlinear cases were computed for investigating the effect of the longitudinal vortices on the mean flow characteristics. The disturbance amplitudes for the later cases were chosen such that the spanwise modulation of the streamwise velocity was approximately

Table 2 Spanwise grid extent, Δz, number of cells in the spanwise direction, and spanwise boundary condition (BC) used for 3-D RANS calculations

Case	Linear	Nonlinear
Δz	0.15	0.3
Cells in z	48	48
BC	Symmetry	Periodicity

Table 3 Inflow disturbances for 3-D RANS calculations [Eqs. (12) and (13)]: linear and nonlinear (NL) cases

Case	$k_{\max}$	A_k	Φ_k
Linear	6	$A_k = 10^{-6}$	$\Phi_{1...6} = 0$ deg
NL 1a	2	$A_k = 0.001$	$\Phi_{1,2} = 0$ deg
NL 1b	2	$A_k = 0.001$	$\Phi_1 = 0$ deg, $\Phi_2 = 90$ deg
NL 2a	2	$A_k = 0.01$	$\Phi_{1,2} = 0$ deg
NL 2b	2	$A_k = 0.01$	$\Phi_1 = 0$ deg, $\Phi_2 = 90$ deg
NL 3a	2	$A_k = 0.05$	$\Phi_{1,2} = 0$ deg
NL 3b	2	$A_k = 0.05$	$\Phi_1 = 0$ deg, $\Phi_2 = 90$ deg

of the same size as in the experiments by Wygnanski and coworkers [3,4], where vortex generators were placed at the nozzle lip for introducing streamwise disturbances into the flow. The spanwise modulation of the streamwise velocity observed in the experiment was about 15–20%. The maximum spanwise modulation obtained from the RANS calculations with KW88 model was 0.4% (at $\vartheta = 98$ deg) for cases NL 1a and b, 4% (at $\vartheta = 95$ deg) for cases NL 2a and b, and 15% (at $\vartheta = 71$ deg) and 13% (at $\vartheta = 179$ deg) for cases NL 3a and b, respectively.

The computed circumferential velocity was Fourier-decomposed in the spanwise direction,

$$v_\vartheta = \sum_k v_\vartheta^{(k)} \cos\left(\frac{2\pi k z}{0.3} - \varphi^{(k)}\right) \tag{14}$$

where $v_\vartheta^{(k)}$ and $\varphi^{(k)}$ are amplitude and phase of mode k. Mode $k = 0$ is the spanwise average of the solution. In Fig. 15 the wall-normal integral of the square of the circumferential disturbance velocity (criterion 3 in [8], p. 389),

$$\int (v_\vartheta^{(k)})^2 \, dy \tag{15}$$

is plotted versus the downstream coordinate for the fundamental, $k = 1$, and several higher harmonics. It should be noted that, due to the nonparallel nature of the wall jet, the measure of instability depends on the disturbance quantity being tracked (i.e., the "criterion," see [8]). The computed individual mode amplitude distributions qualitatively follow the behavior explained earlier (Fig. 13). Mode 1 is strongly damped for $\vartheta < 20$ deg and then amplified in the interval $20 < \vartheta < 150$ deg, mode 2 is amplified up to $\vartheta \approx 80$ deg, and so on. The disturbance amplitude of mode k attains its maximum value at the downstream location, ϑ, where the spanwise wavelength, $\lambda_z^{(k)} = 0.3/k$, is roughly equal to the local wall jet half-width (Fig. 16) [5]. This result does not serve as a validation of the RANS results with the experimental data. It does, however, indicate that the physical mechanism responsible for the identical observations is likely the same.

The picture changes when the forcing amplitudes (and as a consequence the intensity of the longitudinal vortices) are gradually increased (Fig. 17). For the following results, only modes 1 and 2 were forced. In all instances, the mode 1 disturbance is initially damped. (Transient and/or nonmodal growth phenomena as discussed in, e.g., Joshi and Tumin [7] are not addressed in this paper.) The locations where the mode amplitudes reach their maxima are shifted upstream when the forcing amplitude is increased, indicating nonlinear effects and mode saturation. As the forcing amplitude approaches 1% of the nozzle exit jet velocity, the relative phase shift Φ_k begins to have an effect on the mode amplitude distribution. This becomes especially clear for $A_k = 0.05$: When mode 2 is forced phase shifted by 90 deg relative to mode 1, mode 1

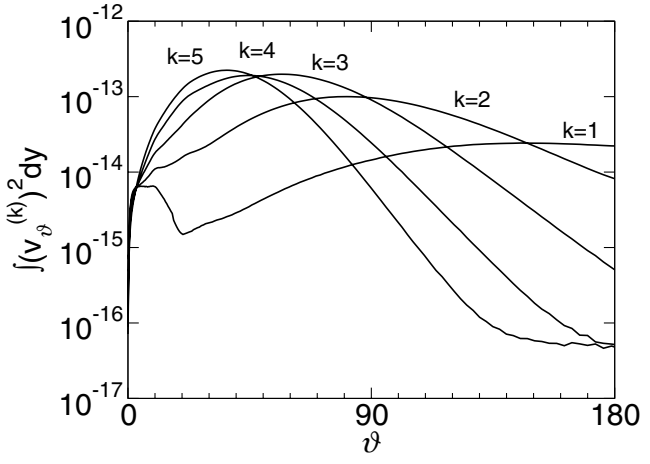

Fig. 15 3-D RANS. Linear case. Disturbance amplitudes.

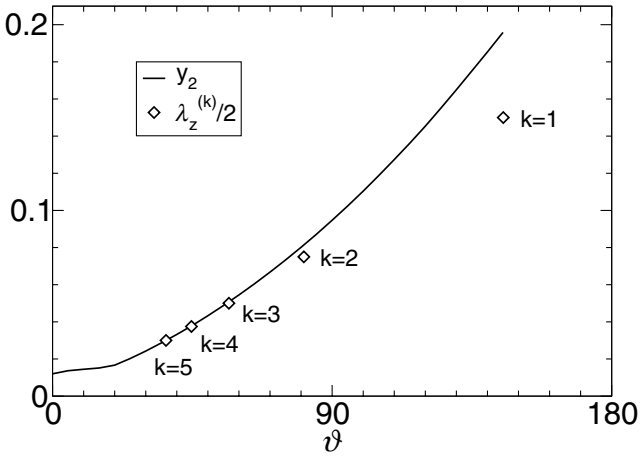

Fig. 16 3-D RANS. Linear case. Wall jet half-width plotted over downstream location. Spanwise wavelength of mode *k* plotted over downstream location, where mode *k* amplitude reaches maximum value (Fig. 15).

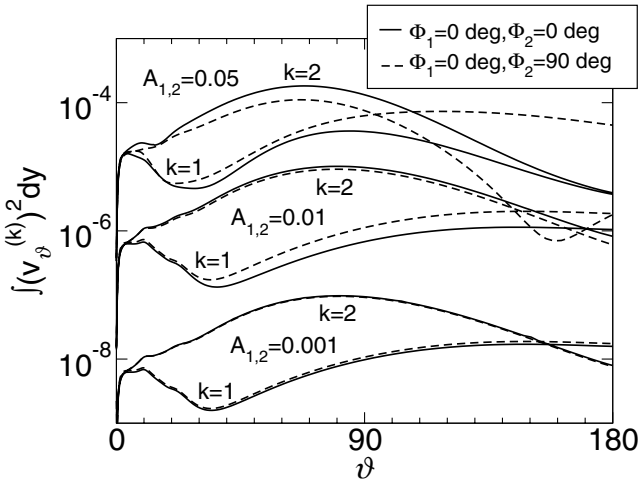

Fig. 17 3-D RANS. Nonlinear cases. Disturbance amplitudes for three different forcing amplitudes, A_k.

is amplified over a larger downstream interval. Mode 2 is less amplified for $\vartheta < 80$ deg and experiences stronger damping for $\vartheta > 80$ deg. We conjecture that for the phase-shifted case subharmonic resonance provides for a sustained energy transfer from the fundamental ($k = 2$) to the subharmonic ($k = 1$).

A 3-D visual impression of the differences between the nonlinear cases 3a and b is given in Fig. 18. Shown are isosurfaces of streamwise vorticity, ω_ϑ. When modes 1 and 2 are forced in phase, mode 2 maintains a larger disturbance amplitude than mode 1 up to $\vartheta = 180$ deg. When modes 1 and 2 are forced with a relative phase shift of 90 deg, the mode 1 disturbance amplitude surpasses the mode 2 amplitude for $\vartheta > 90$ deg. In the 3-D visualization (Fig. 18) this behavior has the appearance of a "vortex merging." Visualizations of the streamwise velocity at two different downstream locations are shown in Fig. 19. When modes 1 and 2 are forced in phase, mode 2 remains dominant and four streamwise vortices are located within the computational domain at both streamwise locations, indicated by three maxima of the streamwise velocity in Fig. 19. When modes 1 and 2 are forced with a phase shift of 90 deg, two of the three maxima are moving closer to each other indicating a vortex merging.

As a consequence of the additional momentum exchange due to the streamwise vortices the wall jet half-width is slightly increased (Fig. 20) when the forcing amplitude is large enough. Forcing amplitudes of 0.01 and 0.001 had no noticeable effect on the wall jet half-width. As another criterion for the intensity of the streamwise

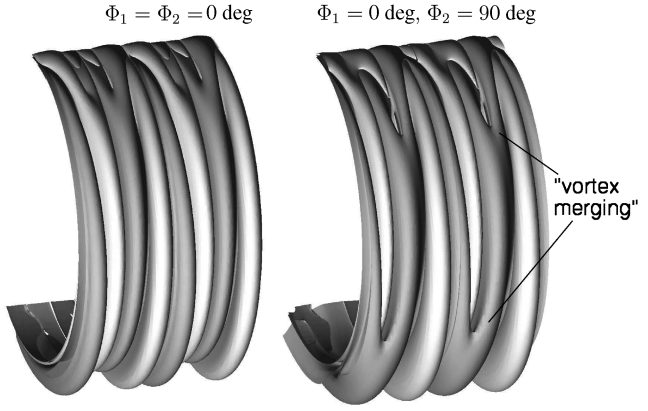

Fig. 18 3-D RANS. Nonlinear cases 3a and b. Isosurfaces −0.2 and 0.2 of streamwise vorticity, ω_ϑ. Nozzle exit is on top. The computational domain was extended once in the spanwise direction.

vortices, the total circulation in the (r, z)-plane can be computed for each downstream location,

$$\Gamma(\vartheta) = \int_{y=0}^{\infty} \int_{z=0}^{0.3} |\omega_\vartheta| \mathrm{d}z\, \mathrm{d}y \tag{16}$$

Results are shown in Fig. 21. The circulation first decays up to $\vartheta \approx 35$ deg. It then reaches a maximum around $\vartheta \approx 90$ deg. When comparing with Fig. 17 it can be seen that the locations of these maxima approximately correspond to the locations where the mode 2 disturbance amplitudes reach their maxima. For $A_k = 0.05$, the decay of total circulation for $\vartheta = 90$ deg is noticeably reduced when mode 1 and mode 2 are forced with a phase shift of 90 deg. For $A_k = 0.05$, the additional mixing introduced by the vortices also modifies the wall jet velocity profiles away from the wall, making them "fuller" beyond the maximum velocity location and increasing the slope at the inflection point (Fig. 22). Forcing amplitudes of 0.01 and 0.001 had no noticeable impact on the velocity profiles.

To check if the spanwise grid resolution was sufficient, the number of cells in the spanwise direction was doubled while the spanwise extent of the computational domain was kept constant at $\Delta z = 0.3$. Figure 23 shows a comparison for the nonlinear cases 3a and b, which have the largest disturbance amplitudes and thus the largest spanwise gradients in the solution and thus require the finest spanwise grid resolution. The differences in the computed results were considered small enough for the purpose of the present investigations.

Finally, 3-D RANS calculations were also carried out with the KW98 model. With this model, the wall jet spreading and velocity decay rate were noticeably underpredicted (Fig. 8). The predicted Görtler numbers were, however, larger than for the KW88 model (Fig. 13) which should result in a stronger centrifugal instability. In fact, significantly larger amplification rates were computed with the KW98 model (Fig. 24), resulting in mode disturbance amplitudes that were one order of magnitude larger than for the KW88 model for the same forcing amplitudes (Fig. 17). Also, mode 1 was not damped

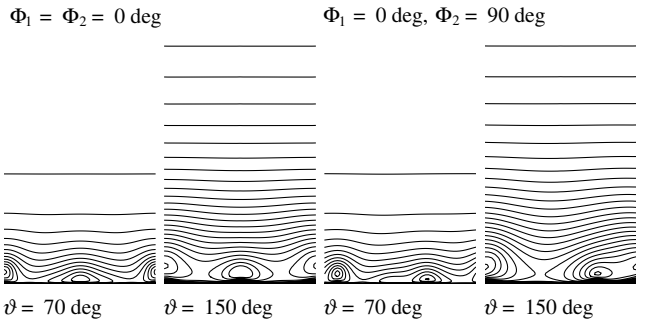

Fig. 19 3-D RANS. Nonlinear cases 3a and b. Isocontourlines of streamwise velocity in planes of constant ϑ. Contour level increment 0.04 ($\vartheta = 70$ deg) and 0.01 ($\vartheta = 150$ deg).

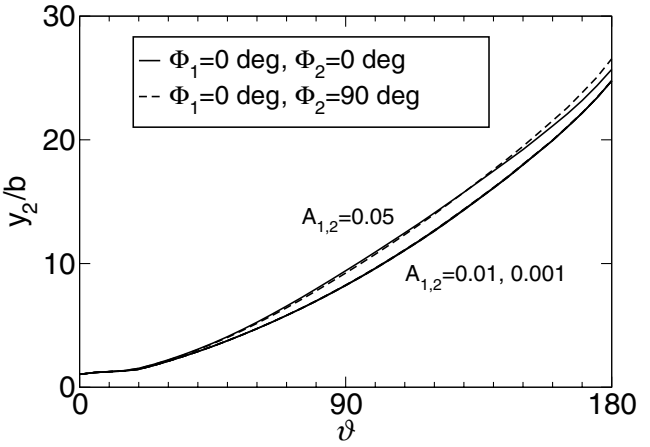

Fig. 20 3-D RANS. Nonlinear cases. Wall jet half-width (spanwise average) for three different forcing amplitudes, A_k.

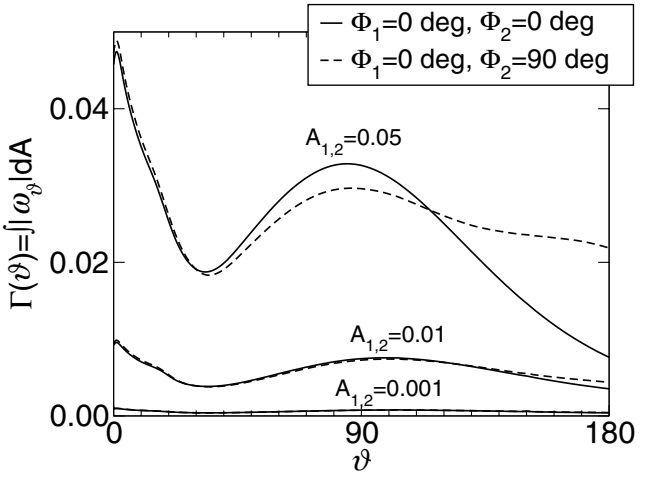

Fig. 21 3-D RANS. Nonlinear cases. Total circulation in planes of constant ϑ for three different forcing amplitudes, A_k.

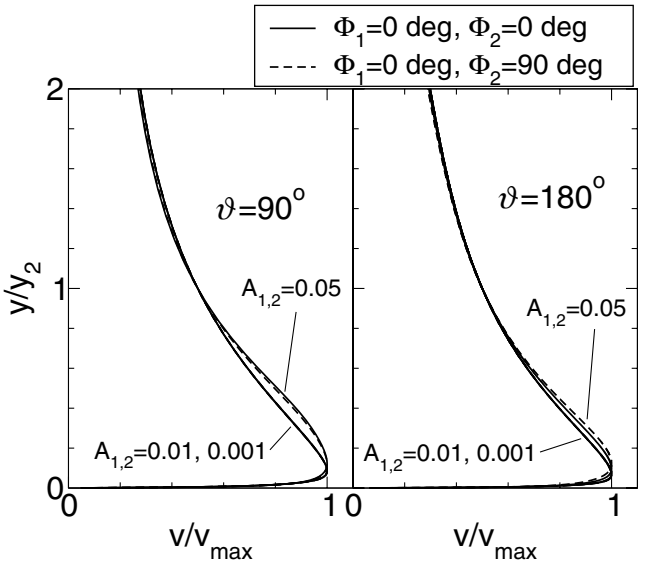

Fig. 22 3-D RANS. Nonlinear cases. Wall-normal profiles of streamwise velocity (spanwise average) for three different forcing amplitudes, A_k.

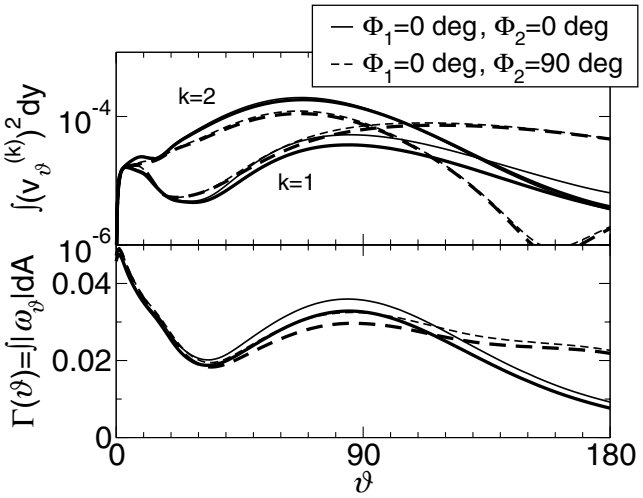

Fig. 23 3-D RANS. Nonlinear cases. Disturbance amplitudes and total circulation for $A_{1,2} = 0.05$. Results obtained with 48 (thick lines) and 96 cells (thin lines) in the spanwise direction.

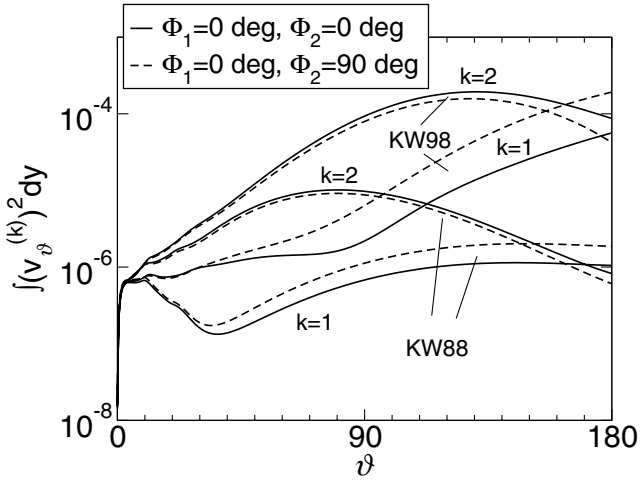

Fig. 24 3-D RANS. Nonlinear cases, $A_{1,2} = 0.01$. Disturbance amplitudes.

for $\vartheta < 35$ deg when the KW98 model was employed. The maximum spanwise modulation observed in the RANS calculations with KW98 model was 20% (at $\vartheta = 179$ deg) and 15% (at $\vartheta = 179$ deg) for cases NL 2a and b, respectively. It can be concluded that a correct prediction of the velocity and eddy-viscosity profiles in the 2-D RANS precursor calculations is a crucial prerequisite before any quantitative statement about the centrifugal instability of the turbulent Coanda wall jet with respect to streamwise vortices can be made.

Discussion

Two-dimensional RANS calculations of a Coanda wall jet experiment by Wygnanski and coworkers [1–5] were conducted with a variety of turbulence models, specifically the 1988 and 1998 Wilcox k–ω models, the Menter SST model, the Lam–Bremhorst low-Reynolds number k–ε model, and the Spalart–Allmaras model. All of these models were used in combination with the Boussinesq–approximation. For the 1998 k–ω model the Reynolds stresses were also computed with an explicit algebraic stress model (EASM) by Rumsey and Gatski [27]. None of the 2-D RANS calculations provided results that fully reproduced quantitatively the experimental data in terms of predicted rates of wall jet spreading and wall jet velocity decay and predicted velocity profiles. The differences in the computed profiles of turbulence intensity and Reynolds shear stress were also relatively large. A number of explanations for these discrepancies are possible: First and foremost, turbulent Coanda flows are difficult to predict due to the physical complexity of the flow (presence of large structures, etc.) The observed and measured behavior strongly depends on the "initial condition" (i.e., what comes out of the nozzle) which is typically not documented in the experiments. The assumptions made for the nozzle outflow conditions (the decision was made to not model the flow in the nozzle but rather prescribe the nozzle outflow conditions) may be one possible explanation for the mismatch between the computed results and the experimental data. For fixed laminar inflow conditions (as chosen for the current investigations) the downstream development of the jet is strongly dependent on how the transition process is emulated by the turbulence models. The large differences between the various results are not surprising because turbulence models are generally not designed or suited for computing through transition. Linear eddy-viscosity models do not account for the effect of flow curvature on the turbulence characteristics. Results obtained with 1998 k–ω model with Boussinesq–approximation (linear closure) and EASM (second-moment closure) were not considerably different from each other, indicating that curvature effects were less important for the current case. A clear decision regarding the significance of the complexity of the turbulence closure or curvature correction terms could, however, not be made because the transition was also computed differently by the two approaches. Freestream (or ambient) velocity and turbulence as well as geometric obstructions of the flow in vicinity of the Coanda cylinder can also influence the downstream development of the wall jet. Finally, the suppression of 3-D structures, whose existence are supported by ample experimental evidence [2–4] and which add to the wall-normal momentum exchange, may also explain some of the shortcomings of the 2-D RANS results.

Because it was shown by Wygnanski and coworkers [1–5] that streamwise vortical structures persisted in the turbulent wall jet, it was decided to study the evolution of streamwise vortical structures in the turbulent wall jet using steady 3-D RANS. The present investigations were based on the 2-D RANS results obtained with the 1988 k–ω linear eddy-viscosity model (which predicted the best match of wall jet spreading and velocity decay rate with the measurements). Because of the severe deficiencies of the 2-D RANS modeling approach described earlier, the 3-D RANS results have to be interpreted in a purely qualitative manner. The findings are, nevertheless, physically meaningful and may help understand some of the aspects of streamwise vortices in turbulent Coanda wall jet flows. In the 3-D RANS calculations the vortical structures were forced at the nozzle exit (inflow of computational domain). For a certain range of spanwise wavelengths of the streamwise vortices it was shown that these vortices could grow in the downstream direction. This growth was attributed to a centrifugal Görtler-type instability of the turbulent Coanda wall jet. To obtain a clearer understanding of the downstream evolution of the vortex structures, the solution was decomposed into spanwise Fourier modes. For low forcing amplitudes (linear case) modes with a spanwise wavelength λ_z were shown to reach their maximum amplitude at the downstream location where the half-width was roughly equal $\lambda_z/2$ [5,7]. The behavior changed when the structures were forced at larger, nonlinear amplitudes: As the forcing amplitudes were increased the spanwise modes attained their peak amplitudes earlier and the relative phase of the modes became important. Significantly different mode disturbance amplitudes were computed when subharmonic and fundamental were forced with a phase shift of 90 deg. The predicted amplification rates were weak, indicating that the flow in the 3-D RANS with 1988 k–ω model was only marginally Görtler unstable. Considerably larger amplification rates were computed in separate 3-D RANS calculations with 1998 k–ω model. This was shown to be mainly a consequence of the lower eddy-viscosity levels predicted with the 1998 k–ω model.

Conclusions

In summary, accurate and reliable RANS predictions of turbulent Coanda wall jet flows appear to be very dependent on the boundary

conditions (jet inflow) and the accurate modeling of the transition process. Especially the latter requirement is beyond the scope of today's turbulence models. No clear statement can be made regarding the applicability of the various turbulence models because the transition was not fixed in the current investigations because it was not known from the experiments. Of the various models that were studied, the k–ω turbulence models seemed to be better suited for steady 2-D RANS calculations of turbulent Coanda wall jets. Three-dimensional RANS calculations showed that the turbulent mean flow can support and amplify streamwise vortices. For steady 2-D RANS the neglect of these coherent structures may also be a contributing factor for the observed discrepancy between calculations and experiments.

Acknowledgment

The authors gratefully acknowledge the Office of Naval Research for the funding of this research under grant number N00014-01-1-09 with Ronald Joslin serving as program manager.

References

[1] Neuendorf, R., and Wygnanski, I., "On a Turbulent Wall Jet Flowing over a Circular Cylinder," *Journal of Fluid Mechanics*, Vol. 381, 1999, pp. 1–25.

[2] Neuendorf, R., "Turbulent Wall Jet Along a Convex Curved Surface," Ph.D. Dissertation, Univ. of Berlin, Berlin, 2000.

[3] Cullen, L. M., Han, G., Zhou, M. D., and Wygnanski, I., "On the Role of Longitudinal Vortices in Turbulent Flow over a Curved Surface," AIAA Paper 2002-2828, June 2002.

[4] Han, G., Zhou, M. D., and Wygnanski, I., "Streamwise Vortices in a Turbulent Wall Jet Flowing over a Circular Cylinder," AIAA Paper 2004-2350, June–July 2004.

[5] Likhachev, O., Neuendorf, R., and Wygnanski, I., "On Streamwise Vortices in a Turbulent Wall Jet that Flows over a Convex Surface," *Physics of Fluids*, Vol. 13, No. 6, 2001, pp. 1822–1825.

[6] Pajayakrit, P., and Kind, R. J., "Streamwise Vortices in the Outer Layer of Wall Jets with Convex Curvature," *AIAA Journal*, Vol. 37, No. 2, 1999, pp. 281–283.

[7] Joshi, H., and Tumin, A., "Centrifugal Instability in a Turbulent Wall Jet over a Circular Cylinder," AIAA Paper 2004-1108, Jan. 2004.

[8] Saric, W. S., "Görtler Vortices," *Annual Review of Fluid Mechanics*, Vol. 26, 1994, pp. 379–409.

[9] Swearingen, J. D., and Blackwelder, R. F., "The Growth and Breakdown of Streamwise Vortices in the Presence of a Wall," *Journal of Fluid Mechanics*, Vol. 182, 1987, pp. 255–290.

[10] Liu, W., and Domaradzki, J. A., "Direct Numerical Simulation of Transition to Turbulence in Görtler Flow," *Journal of Fluid Mechanics*, Vol. 246, 1993, pp. 267–299.

[11] Tani, I., "Production of Longitudinal Vortices in the Boundary Layer Along a Concave Wall," *Journal of Geophysical Research*, Vol. 67, No. 8, 1962, pp. 3075–3080.

[12] Moser, R. D., and Moin, P., "The Effects of Curvature in Wall-Bounded Turbulent Flows," *Journal of Fluid Mechanics*, Vol. 175, 1987, pp. 479–510.

[13] Wernz, S. H., Valsecchi, P., Groß, A., and Fasel, H. F., "Numerical Investigation of Transitional and Turbulent Wall Jets Over a Convex Surface," AIAA Paper 2003-3727, June 2003.

[14] Wernz, S. H., Gross, A., and Fasel, H. F., "Numerical Investigation of Coherent Structures in Plane and Curved Wall Jets," AIAA Paper 2005-4911, June 2005.

[15] Wernz, S. H., "Numerical Investigation of Forced Transitional and Turbulent Wall Jets," Ph.D. Dissertation, Univ. of Arizona, Tucson, AZ, 2001.

[16] Pajayakrit, P., and Kind, R. J., "Assessment and Modification of Two-Equation Turbulence Models," *AIAA Journal*, Vol. 38, No. 6, 2000, pp. 955–963.

[17] Kline, S. J., Cantwell, B. J., and Lilley, G. M. (eds.), "Comparison of Computation with Experiment, and Computers' Summary Reports," *Proceedings from the 1980-81 AFOSR-HTTM-Stanford Conference on Complex Turbulent Flows: Comparison of Computation and Experiment*, Vol. 3, Thermosciences Division, Mechanical Engineering Dept., Stanford Univ., Stanford, CA, 1982.

[18] Spalart, P. R., and Shur, M., "On the Sensitization of Turbulence Models to Rotation and Curvature," *Aerospace Science and Technology*, Vol. 1, No. 5, 1997, pp. 297–302.

[19] Rumsey, C. L., Gatski, T. B., Anderson, W. K., and Nielsen, E. J., "Isolating Curvature Effects in Computing Wall-Bounded Turbulent Flows," *International Journal of Heat and Fluid Flow*, Vol. 22, No. 6, 2001, pp. 573–582.

[20] Swanson, R., Rumsey, C., and Sanders, S., "Progress Towards Computational Method for Circulation Control Airfoils," AIAA Paper 2005-89, Jan. 2005.

[21] Slomski, J. F., Gorski, J. J., Miller, R. W., and Marino, T. A., "Numerical Simulation of Circulation Control Airfoils as Affected by Different Turbulence Models," AIAA Paper 2002-0851, Jan. 2002.

[22] Wilcox, D. C., *Turbulence Modeling for CFD*, 2nd ed., DCW Industries, La Cañada, CA, 2000.

[23] Menter, F. R., "2-Equation Eddy-Viscosity Turbulence Models for Engineering Applications," *AIAA Journal*, Vol. 32, No. 8, 1994, pp. 1598–1605.

[24] Menter, F. R., "Influence of Freestream Values on k–ω Turbulence Model Predictions," *AIAA Journal*, Vol. 30, No. 6, 1992, pp. 1657–1659.

[25] Lam, C. K. G., and Bremhorst, K. A., "Modified Form of the k–ε Model for Predicting Wall Turbulence," *Journal of Fluids Engineering*, Vol. 103, No. 3, 1981, pp. 456–460.

[26] Spalart, P. R., and Allmaras, S. R., "A One-Equation Turbulence Model for Aerodynamic Flows," AIAA Paper 92-0439, Jan. 1992.

[27] Rumsey, C. L., and Gatski, T. B., "Recent Turbulence Model Advances Applied to Multielement Airfoil Computations," *Journal of Aircraft*, Vol. 38, No. 5, 2001, pp. 904–910.

[28] Gross, A., and Fasel, H. F., "High-Order WENO Schemes Based on the Roe Approximate Riemann Solver," AIAA Paper 2002-2735, June 2002.

[29] Yee, H. C., "Upwind and Symmetric Shock-Capturing Schemes," NASA Ames Research Center, NASA Technical Memorandum 89464, Moffet Field, CA, May 1987.

[30] Dejoan, A., and Leschziner, M. A., "Large Eddy Simulation of a Plane Turbulent Wall Jet," *Physics of Fluids*, Vol. 17, No. 2, 2005, pp. 025102-1–025102-16.

[31] Gross, A., Wernz, S., and Fasel, H. F., "Numerical Investigation of Coherent Structures in a Turbulent Coanda Wall Jet," AIAA Paper 2003-4020, June 2003.

[32] Gross, A., and Fasel, H. F., "Numerical Investigation of Streamwise Coherent Structures in a Turbulent Coanda Wall Jet," AIAA Paper 2004-2346, June–July 2004.

[33] Wilcox, D. C., "Simulation of Transition with a 2-Equation Turbulence Model," *AIAA Journal*, Vol. 32, No. 2, 1994, pp. 247–255.

[34] Kim, J. W., and Lee, D. J., "Generalized Characteristic Boundary Conditions for Computational Aeroacoustics," *AIAA Journal*, Vol. 38, No. 11, 2000, pp. 2040–2049.

K. Ghia
Associate Editor